

## Part IIB Project 2019/20

### Technical Abstract

#### Computations in Neural Circuits

Yuetong Chen

Sidney Sussex College

---

This project aims to gain understanding of across-trial variability in the multi-attractor model. It has been shown that stimulus onset causes a decline in trial-to-trial variability of neuronal activity. Several dynamical mechanisms have been purposed to model variability suppression and they exhibit different dynamical behaviours. As one of mechanisms, the multi-attractor model shows an initial variability increase at stimulus onset before variability drops (Hennequin et al., 2018). The multi-attractor model has been used to model a range of neuronal activities. This unique variability behaviour could be a key to identify the multi-attractor dynamics in studying cortical areas, yet the details and robustness has not been confirmed. This report describes procedures to perform numerical simulations of the ring attractor model as well as methods to model simulated membrane potentials as circular Gaussian bumps. Statistics of bump parameters, including the first moment and the second moment, are used to model the across-trial variance.

The ring attractor model is composed of neurons with preferred orientation varied around a ring. The external input is the sum of a constant baseline and an angular modulated component. The external noise is modelled as a Ornstein-Uhenbeck process and is both spatially and temporally correlated. The external input and noise are presented to each neuron of which the firing rate is given by a non-linearity of its membrane potential. The network and noise dynamical differential equations are simulated with the forward Euler scheme. Simulated neuronal activity and variability dynamics matched the previously published results in terms of magnitude and timescale (Hennequin et al., 2018), supporting the correctness of our implemented model.

The bump of stimulus-driven input drives bumps of network response, so we fit a function of circular Gaussian (“bump”) with four variables, including bump amplitude, location, width and baseline, to the network activity. The ‘free model’ optimisation estimates all four variables independently at each time point, while the ‘fixed model’ optimisation constrains the bump baseline to be constant for all time points in a phase (i.e. spontaneous/evoked activity). Two models are validated on synthetic data and applied to the simulated membrane potentials. It is found that the fixed model has limited ability to model network activity caused by the constraint in bump baseline. The free model optimisation is used to estimate parameter values and perform further analysis.

Statistics of bump parameters are used to model the across-trial variability. The across-trial variance is reconstructed by the first moment and the second moment of the bump parameters under assumptions on bump and temporal dynamics. Validity of each assumption is qualitatively tested by examining accuracy of reconstructed variance to true variance under a single assumption or a combination of assumptions. We found that the across-trial variability in the ring attractor model is mainly caused by the spatial and temporal dynamics of bump amplitude and variance of bump location. At stimulus onset, the amplitude of activity bump increases in a short time scale while the variance of bump location drops slowly due to movement from a random angular location to the stimulus orientation. The across-trial variance, which is proportional to the product of two terms, then shows an initial peak before its magnitude decreases.

# Contents

<b>1</b>	<b>Introduction and Aims</b>	<b>5</b>
1.1	Theoretical Background . . . . .	5
1.2	Project Aims . . . . .	6
<b>2</b>	<b>Variability Quenching in Ring Attractor Model</b>	<b>7</b>
2.1	Network Dynamics Simulations . . . . .	7
2.1.1	Model Architecture . . . . .	7
2.1.2	Network Simulations . . . . .	9
2.2	Network Dynamics and Variability Quenching . . . . .	10
<b>3</b>	<b>Modelling Network Dynamics with Gaussian Bumps</b>	<b>11</b>
3.1	Least Squares Fitting of Circular Gaussian . . . . .	11
3.2	Bump Fit of Network Activity . . . . .	16
<b>4</b>	<b>Network Dynamics and Variability Modelling</b>	<b>18</b>
4.1	Statistics of Bump Parameters . . . . .	18
4.2	Variability Modelling with Bump Parameters . . . . .	20
4.3	Relations to Network Dynamics . . . . .	22
<b>5</b>	<b>Future Work</b>	<b>25</b>
5.1	Large Scale Simulations . . . . .	25
5.2	Generalising Analysis . . . . .	26
<b>6</b>	<b>Conclusions</b>	<b>26</b>
<b>7</b>	<b>Appendix</b>	<b>27</b>
7.1	Network Parameters Used in Numerical Simulations . . . . .	27
7.2	Mathematical Formulations . . . . .	27
7.2.1	The Forward Euler Scheme . . . . .	27
7.2.2	Partial Derivatives of Objective Function to Bump Variables . . . . .	27
7.3	Data and Software Availability . . . . .	28
7.4	Health and Safety Retrospective . . . . .	28
7.5	COVID-19 Disruption . . . . .	28
	<b>References</b>	<b>29</b>

## Acknowledgements

I would like to express my great appreciation to Professor Máté Lengyel for supervising me on this project and for all the meetings in the past academic year. The project work including numerical simulations, optimisation algorithms and theory of variance modelling would not have been possible without his exceptional support and guidance. I also extend my thanks to Dr Marcelo Mattar for kindly having the discussions to help me understand model architecture and implementation.

# 1 Introduction and Aims

## 1.1 Theoretical Background

In neuroscience, a fundamental approach to study neuronal activity is to use electrodes to record the electrical potential of neurons. Recorded responses are highly variable across trials even the stimulus presented is the same. A classical approach is to average the neural responses over repeated stimulus trials, which aims to reduce the effect of noises. Recently, it has been shown that the presence of stimulus causes a decline in trial-to-trial variability of membrane potentials across a wide range of cortical areas (Churchland et al., 2010). Second-order statistics of neural activity can carry information in encoding of stimulus (Ponce-Alvarez et al., 2013). The underlying network mechanism of cortical circuits can be studied from stimulus-induced reduction of variability.

Several dynamical mechanisms have been proposed to model stimulus quenching of cortical activities, including the multi-attractor model, the chaos suppression model and the stochastic stabilized supralinear network model (Hennequin et al., 2018). Each mechanism exhibits a different dynamical behaviour of variability quenching. As one of the mechanisms, the multi-attractor model shows an initial variability increase at stimulus onset before the variability drops. This pattern is fundamentally different from the direct quenching of variability in the chaos suppression model and the stochastic SSN model.

The multi-attractor network is a type of recurrent network that have multiple stable states (“attractors”). The multi-attractor model has been used to model a range of neuronal activities:

- Tuning of neuronal responses to the stimulus orientation in primary visual cortex (V1) and middle temporal (MT) visual area (Ben-Yishai et al., 1995; Ponce-Alvarez et al., 2013).
- Patterns of neuronal activity during working memory related tasks (Seung, 1996; Wimmer et al., 2014).
- Tuning of firing rates to the preferred firing direction in head direction cells (Zhang, 1996; Kim et al., 2017).

The dynamics of variability could be a feature to identify multi-attractor dynamics in studying cortical areas. The initial variance increase differentiates multi-attractor dynamics to other purposed dynamics, yet its details and robustness has not been confirmed by other studies.

## 1.2 Project Aims

In this project, we aim to understand dynamics of across-trial variance in the multi-attractor network. This include:

- Gain intuitive understanding of network dynamics by performing numerical simulations and modelling with circular Gaussian bumps.
- Study the dynamical mechanism of variability suppression using bump parameters.

## 2 Variability Quenching in Ring Attractor Model

### 2.1 Network Dynamics Simulations

#### 2.1.1 Model Architecture

An architecture in which the preferred stimulus of neurons varied around a ‘ring’ (“ring attractor model”) is used in our study (Figure 1A). The ring attractor model has been proposed to model the statistics of neural activity for MT neurons (Ponce-Alvarez et al., 2013).

The ring attractor model is governed by the network dynamics equation as

$$\tau_m \frac{dV_i(t)}{dt} = -V_i(t) + h_i(t) + \eta_i(t) + \sum_j W_{ij} r(V_j(t)) \quad (1)$$

where  $V_i(t)$  denotes the membrane potential of neuron  $i$ ,  $r(V_j(t))$  denotes the momentary firing rate of neuron  $j$ ,  $\tau_m$  is the membrane time constant,  $W_{ij}$  is the strength of synaptic connection from neuron  $j$  to neuron  $i$ , and  $h_i(t)$  is the external input to which a noise term  $\eta_i(t)$  is added. The preferred orientation  $\theta$  of each neuron varies from  $-180^\circ$  to  $180^\circ$ .

The network is composed of  $N$  neurons with connectivity  $W_{ij}$  (Figure 1B)

$$W_{ij} = \frac{1}{N} [\bar{W} + W_\Delta \cos(\theta_i - \theta_j)] \quad (2)$$

where  $\bar{W}$  and  $W_\Delta$  are two parameters that control the average connection strength and modulation with tuning dissimilarity respectively. Connections between all neuron pairs are inhibitory to keep the system marginally stable.

The momentary firing rate of neuron  $r(V_i)$  is given by a hyperbolic tangent function (non-linearity) of its membrane potential (Figure 1C)

$$r(V_i) = g_{\max} \tanh(k [V_i]_+). \quad (3)$$

The external input  $h_i$  to each neuron (Figure 1D) is the sum of two components

$$h_i = b_0 + c \cdot (1 - A + A \cdot \cos(\theta_i - \theta_{\text{stim}})). \quad (4)$$

The first term is a constant baseline  $b_0$  which drives spontaneous activity. The second term depends on the angular distance between the preferred orientation and stimulus orientation and is scaled by stimulus strength  $c$ .

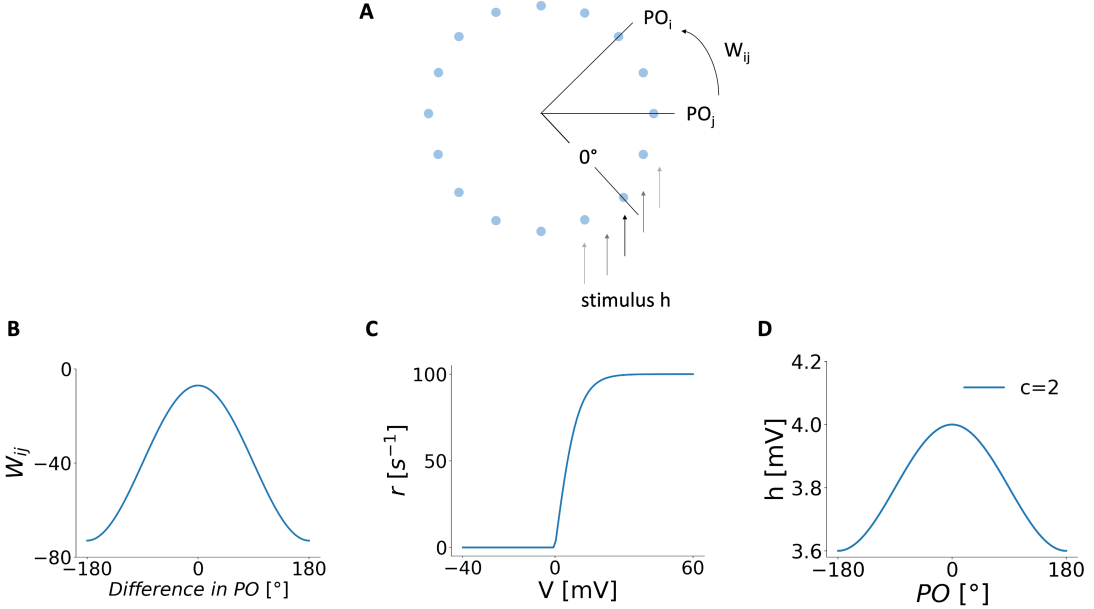


Figure 1: **Architecture of the Ring Attractor Model**

- (A) Schematics of the ring architecture. Neurons arranged on a ring which have angular positions indicating their preferred stimulus orientations; stimulus presented at \$0^\circ\$.
- (B) Synaptic connectivity following a circular Gaussian profile; all connections are inhibitory (negative quantity).
- (C) Non-linear firing rate of spike count with given external potential input.
- (D) External stimulus input composed of a baseline and a contrast-dependent modulated component (\$c = 2\$).

The external noise  $\eta_i$  is modelled as a multi-variant Ornstein-Uhlenbeck process of time constant  $\tau_{\text{noise}}$

$$\tau_{\text{noise}} d\eta = -\eta dt + \sqrt{2 \tau_{\text{noise}} \Sigma^{\text{noise}}} d\varepsilon \quad (5)$$

where  $\varepsilon$  is a collection of  $N$  independent Wiener processes and  $\Sigma^{\text{noise}}$  is an  $N \times N$  input covariance matrix. The noise correlations among neurons decrease with the difference in their preferred orientations following a circular Gaussian

$$\Sigma_{i,j}^{\text{noise}} = \sigma_{\text{noise}}^2 \exp\left(\frac{\cos(\theta_i - \theta_j) - 1}{\ell_{\text{noise}}^2}\right) \quad (6)$$

where the correlation amplitude is scaled as

$$\sigma_{\text{noise}} = \sigma_0 \sqrt{1 + \frac{\tau_m}{\tau_{\text{noise}}}}. \quad (7)$$

Values of all parameters used for simulations were listed in the Table 1 in Appendix. Note that Equation 5 and 6 imply that the external noise is both spatially and temporally correlated.

### 2.1.2 Network Simulations

Numerical simulations of the ring attractor model were performed by the forward Euler scheme (details in Section 7.2.1 in Appendix). The differential equations of network dynamics (Equation 1 and 5) were integrated using the forward Euler scheme.

#### 1. Membrane Potential: $V_i(t)$

We implemented the network architecture as described in Section 2.1.1. The network dynamics equation (Equation 1) can be expressed as

$$\begin{aligned} \frac{dV_i}{dt} &= f(V_i(t), t) \\ &= \frac{1}{\tau_m} \left[ -V_i(t) + h_i(t) + \eta_i(t) + \sum_j W_{ij} r(V_j(t)) \right] \end{aligned} \quad (8)$$

With step size of  $\Delta t$ , the membrane potential is approximated by

$$V_i(t + \Delta t) = V_i(t) + \Delta t \cdot \frac{1}{\tau_m} \left[ -V_i(t) + h_i(t) + \eta_i(t) + \sum_j W_{ij} r(V_j(t)) \right]. \quad (9)$$

#### 2. External Noise: $\eta_i(t)$

The noise dynamics equation (Equation 5) can be expressed as

$$d\eta = -\frac{\eta}{\tau_{\text{noise}}} dt + \sqrt{\frac{2 \Sigma^{\text{noise}}}{\tau_{\text{noise}}}} d\varepsilon. \quad (10)$$

In a Wiener process  $\varepsilon$ , the increment  $d\varepsilon$  has a Gaussian distribution with zero mean and variance of  $dt$ . This can be substituted into the differential equation (Equation 10) by writing as  $d\varepsilon = x \sqrt{dt}$  where  $x$  is generated from the standard normal distribution  $\mathcal{N}(0, 1)$

$$d\eta = -\frac{\eta}{\tau_{\text{noise}}} dt + x \sqrt{\frac{2 \Sigma^{\text{noise}}}{\tau_{\text{noise}}}} \sqrt{dt}. \quad (11)$$

With step size of  $\Delta t$ , the noise process is approximated by

$$\begin{aligned} \eta(t + \Delta t) &= \eta(t) + \Delta\eta \\ &= \eta(t) + \left( -\frac{\eta(t)}{\tau_{\text{noise}}} \Delta t + x \sqrt{\frac{2 \Sigma^{\text{noise}}}{\tau_{\text{noise}}}} \sqrt{\Delta t} \right) \end{aligned} \quad (12)$$

where  $x$  is a collection of  $N$  independent random variables generated from the standard normal distribution  $\mathcal{N}(0, 1)$

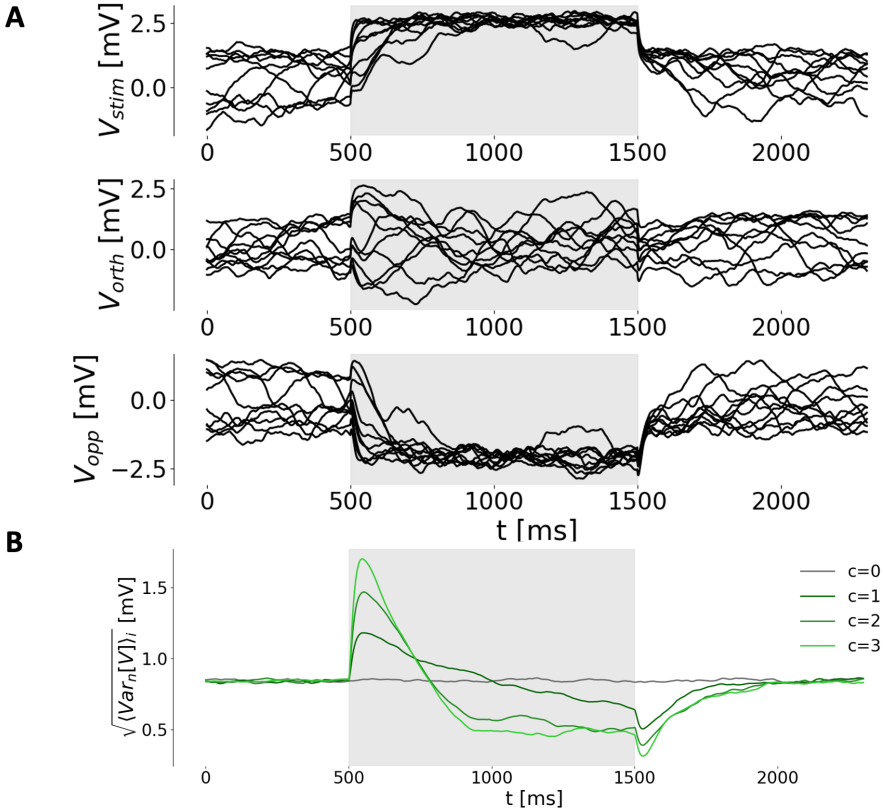


**Figure 2: Variability Quenching in Simulations of Ring Attractor Model**  
(A) Sample membrane potentials ( $N_{\text{trial}} = 10$ ) for a neuron tuned to the stimulus (top), orthogonal (middle) and opposite (bottom) directions. Stimulus applied from 500 milliseconds to 1500 milliseconds for 1 second (grey shading;  $c = 2$ ).  
(B) Standard deviation across trials of membrane potential, averaged across neuron (Equation 13), for different levels of input strength,  $c$  (color coded).

Simulation step size was chosen to be  $\Delta t = 0.1ms$ . The time step was more than 50 times faster than the membrane and noise constant so was sufficient to capture the membrane potential change of neurons in the network.

## 2.2 Network Dynamics and Variability Quenching

Numerical simulations of the ring attractor model as implemented in Section 2.1 were performed at different stimulus level  $c$  (as in Equation 4) for  $N_{\text{trial}}$  times. The across-trial variability  $\bar{\sigma}(t)$  is defined as the across-trial standard deviation of membrane potential averaged across neurons

$$\bar{\sigma}(t) := \sqrt{\langle \text{Var}_n[V_i^n(t)] \rangle_i}, \quad (13)$$

where  $V_i^n(t)$  denotes the membrane potential of neuron  $i$  at time point  $t$  in  $n$ th trial.

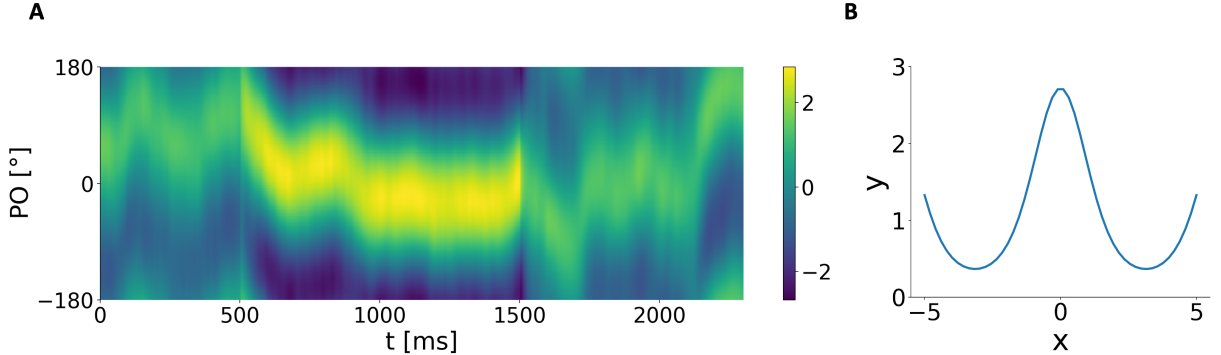


Figure 3: **Modelling Network Activity with Circular Gaussian Function**

(A) Sample membrane potentials of network activity, before, during and after stimulus onset. Stimulus applied from 500 milliseconds to 1500 milliseconds. Neurons are arranged on the y-axis according to their preferred orientations.

(B) Circular Gaussian function  $y = a \cdot \exp\left[\frac{\cos(x-\mu)-1}{w^2}\right] + b$  (parameter values of  $a = 1, \mu = 0, w = 1, b = 0$ ).

Dynamics of network activity and the across-trial variability (Figure 2) were consistent with previously published simulation results under the same parameter settings (Hennequin et al., 2018). Stimulus onset drove the “activity bump” across neurons from a random angular position to match the stimulus orientation (Figure 2A). We also observed the initial variability growth in the presence of stimulus before the variability decreased (Figure 2B). The magnitude and timescale of neuronal activity and variability dynamics matched the previously published results, supporting the correctness of our implemented model.

### 3 Modelling Network Dynamics with Gaussian Bumps

#### 3.1 Least Squares Fitting of Circular Gaussian

In the ring attractor model, the bump of stimulus-driven input (Equation 4) drives a bump of network response during evoked activity (Figure 2A and 3A). To model network activity, the membrane potential  $V_i(t)$  as a function of  $\theta$  across neurons was fitted by a circular Gaussian (“bump”; Figure 3B) at each individual time point in a simulation trial

$$f_i(\boldsymbol{\omega}(t)) = a(t) \cdot \exp\left(\frac{\cos(\theta_i - \mu(t)) - 1}{w(t)^2}\right) + b(t). \quad (14)$$

where bump parameter vector  $\boldsymbol{\omega}(t) = [a(t) \ \mu(t) \ w(t) \ b(t)]^\top$  had four variables – bump amplitude  $a$ , location  $\mu$ , width  $w^2$  and baseline  $b$ . Estimated membrane potential  $\hat{V}_i(t)$  is then computed with the estimated parameter vector  $\hat{\boldsymbol{\omega}}(t)$  at neuron  $i$  and time point  $t$ .

In the bump equation (Equation 14), the bump baseline  $b(t)$  represents the average membrane potential driven by the external input (Equation 4). During spontaneous activity ( $c = 0$ ), the average neuronal activity is purely driven by the constant baseline component

$$\langle h_i(t) \rangle_i = b_0. \quad (15)$$

During evoked activity ( $c \neq 0$ ), the average neuronal activity is driven by the average input of

$$\langle h_i(t) \rangle_i = b_0 + c \cdot (1 - A). \quad (16)$$

The average stimulus input at each time point is constant (Equation 15 and 16) during spontaneous activity before stimulus onset (“pre-stimulus phase”), evoked activity (“evoked phase”) and spontaneous activity after stimulus onset (“post-stimulus phase”). Thus, two models were proposed to model the network activity. In the ‘free model’, we fitted the membrane potentials with parameter vectors estimated independently at each time point. In the ‘fixed model’, the bump baseline  $b$  was constrained to be constant for all time points  $\{T_{\text{start}} \dots T_{\text{end}}\}$  in one phase. Note that the free model can be regarded as the generalisation of the fixed model with baseline  $b(t) = b$  for time points  $t \in \{T_{\text{start}} \dots T_{\text{end}}\}$  in each phase.

Our objective function is the time average of mean squared error of estimator  $\hat{\omega}(t)$  computed at each time point

$$L(\hat{\omega}_{1:T}) = \frac{1}{T} \sum_{t=1}^T MSE(\hat{\omega}(t)) \quad (17)$$

where  $T$  is the total time of one simulation trial. The series of parameter vectors  $\hat{\omega}_{1:T} = \{\hat{\omega}_1 \hat{\omega}_2 \dots \hat{\omega}_T\}$  are required to be estimated at all time points. The mean squared error of estimator  $\hat{\omega}(t)$  is

$$\begin{aligned} MSE(\hat{\omega}(t)) &= \frac{1}{N} \sum_{i=1}^N [V_i(t) - f_i(\hat{\omega}(t))]^2 \\ &= \frac{1}{N} \sum_{i=1}^N \left[ V_i(t) - \hat{a}(t) \cdot \exp \left( \frac{\cos(\theta_i - \hat{\mu}(t)) - 1}{\hat{w}(t)^2} \right) - \hat{b}(t) \right]^2. \end{aligned} \quad (18)$$

The mean squared error  $MSE(\hat{\omega}(t))$  is a non-linear function of parameter vector  $\hat{\omega}(t)$  (Equation 18) so we cannot write it into vector product form. It is not possible to obtain the stationary point from an analytical solution of  $\frac{d MSE(\hat{\omega}(t))}{d\hat{\omega}(t)} = 0$ . Values of the bump variables  $a$ ,  $\mu$ ,  $w^2$  and  $b$  were estimated separately.

The coordinate descent algorithm is applied to find the bump parameter values that minimise the objective function. Iterative approximate minimisation is performed along

four coordinate directions until convergence. In one iteration, the objective function is minimised along each coordinate direction with current values of remaining variables. Different methods were used to optimise four bump variables separately. The partial derivative of objective function with respect to  $\hat{a}$ ,  $\hat{\mu}$  and  $\hat{w}^2$  can be computed at each time point respectively (details in Section 7.2.2 in Appendix). A closed form solution of bump variable  $\hat{a}$  that corresponds to the local minimum of the objection function is derived by solving for  $\frac{\partial L(\hat{\omega}_{1:T})}{\partial \hat{a}} = 0$

$$\hat{a} = \frac{\sum_{i=1}^N (V_i - \hat{b}) \cdot \exp\left(\frac{\cos(\theta_i - \hat{\mu}) - 1}{\hat{w}^2}\right)}{\sum_{i=1}^N \exp\left(\frac{2 \cdot (\cos(\theta_i - \hat{\mu}) - 1)}{\hat{w}^2}\right)}. \quad (19)$$

The values of  $\hat{\mu}$  and  $\hat{w}^2$  that correspond to the local minimum of the objection function cannot be solved analytically and these were estimated by numerical methods. We ensured that the variance of circular Gaussian function  $\hat{w}^2$  is positive. Constrained optimisation was converted into unconstrained optimisation by changing variable  $\hat{w}^2$  to  $\log \hat{w}^2$  and optimising the log value instead. The value of  $b$  was estimated differently for the fixed and free model.

### 1. Free model

In the free model, the coordinate descent algorithm (Algorithm 1) is applied for each time point in one simulation trial independently.

---

#### Algorithm 1 Coordinate Descent for Bump Fitting (Free Model)

---

```

1: procedure COORDINATEDESCENTFREEMODEL
2:    $a, \mu, \log w^2, b \leftarrow$  vectors of random positive floats
3:   repeat
4:     for  $t$  in  $1 : T$  do
5:        $a \leftarrow a'$   $\triangleright \frac{\partial L(a', b, w^2, b)}{\partial a} = 0$ 
6:        $b \leftarrow b'$   $\triangleright \frac{\partial L(a, b', w^2, b)}{\partial b} = 0$ 
7:        $\mu, \log w^2 \leftarrow \arg \min_{\mu, \log w^2} L(\omega)$   $\triangleright$  direct optimization
8:   until convergence.

```

---

Values of all four variables are estimated independently for every time point. There are  $4T$  parameters to estimate in total. The partial derivative of objective function with respect to  $\hat{b}$  can be computed at a time point  $t$  (symbol  $t$  in bump variables and membrane potential is neglected in Equation 20 and 21)

$$\frac{\partial L(\hat{\omega}_{1:T})}{\partial \hat{b}} = -\frac{2}{NT} \sum_{i=1}^N \left[ V_i - \hat{a} \cdot \exp\left(\frac{\cos(\theta_i - \hat{\mu}) - 1}{\hat{w}^2}\right) - \hat{b} \right]. \quad (20)$$

A closed form solution of  $\hat{b}$  that corresponds to the local minimum of the objection function is derived and used to optimise  $\hat{b}$  in Algorithm 1 by solving  $\frac{\partial L(\hat{\omega}_{1:T})}{\partial \hat{b}} = 0$

$$\hat{b} = \frac{1}{N} \sum_{i=1}^N \left[ V_i - \hat{a} \cdot \exp \left( \frac{\cos(\theta_i - \hat{\mu}) - 1}{\hat{w}^2} \right) \right]. \quad (21)$$

## 2. Fixed model

In the fixed model, the coordinate descent algorithm (Algorithm 2) is applied for all time points in one phase.

---

**Algorithm 2** Coordinate Descent for Bump Fitting (Fixed Model)

---

```

1: procedure COORDINATEDESCENTFIXEDMODEL
2:    $a, \mu, \log w^2 \leftarrow$  vectors of random positive floats
3:    $b \leftarrow$  random positive float
4:   for each phase do
5:     repeat
6:        $b \leftarrow b'$   $\triangleright \frac{\partial L(a, b', w^2, b)}{\partial b} = 0$ 
7:       for  $t$  in  $T_{\text{start}} : T_{\text{end}}$  do  $\triangleright$  with current value of  $b$ 
8:          $a \leftarrow a'$   $\triangleright \frac{\partial L(a', b, w^2, b)}{\partial a} = 0$ 
9:          $\mu, \log w^2 \leftarrow \arg \min_{\mu, \log w^2} L(\omega)$   $\triangleright$  direct minimisation
10:    until convergence.

```

---

A single value of  $b$  is estimated for all time points in one phase. Values of  $a, \mu, w^2$  are estimated at each time point. There were  $3T+3$  parameters to estimate in total. The partial derivative of objective function with respect to  $\hat{b}$  can be computed

$$\frac{\partial L(\hat{\omega}_{1:T})}{\partial \hat{b}} = -\frac{2}{N(T_{\text{end}} - T_{\text{start}})} \sum_{i=1}^N \sum_{t=T_{\text{start}}}^{T_{\text{end}}} \left[ V_i(t) - \hat{a}(t) \cdot \exp \left( \frac{\cos(\theta_i - \hat{\mu}(t)) - 1}{\hat{w}(t)^2} \right) - \hat{b} \right]. \quad (22)$$

A closed form solution of  $\hat{b}$  in each phase that corresponds to the local minimum of the objection function was derived and used to optimise  $\hat{b}$  in Algorithm 2 by solving  $\frac{\partial L(\hat{\omega}_{1:T})}{\partial \hat{b}} = 0$

$$\hat{b} = \frac{1}{N(T_{\text{end}} - T_{\text{start}})} \sum_{i=1}^N \sum_{t=T_{\text{start}}}^{T_{\text{end}}} \left[ V_i(t) - \hat{a}(t) \cdot \exp \left( \frac{\cos(\theta_i - \hat{\mu}(t)) - 1}{\hat{w}(t)^2} \right) \right]. \quad (23)$$

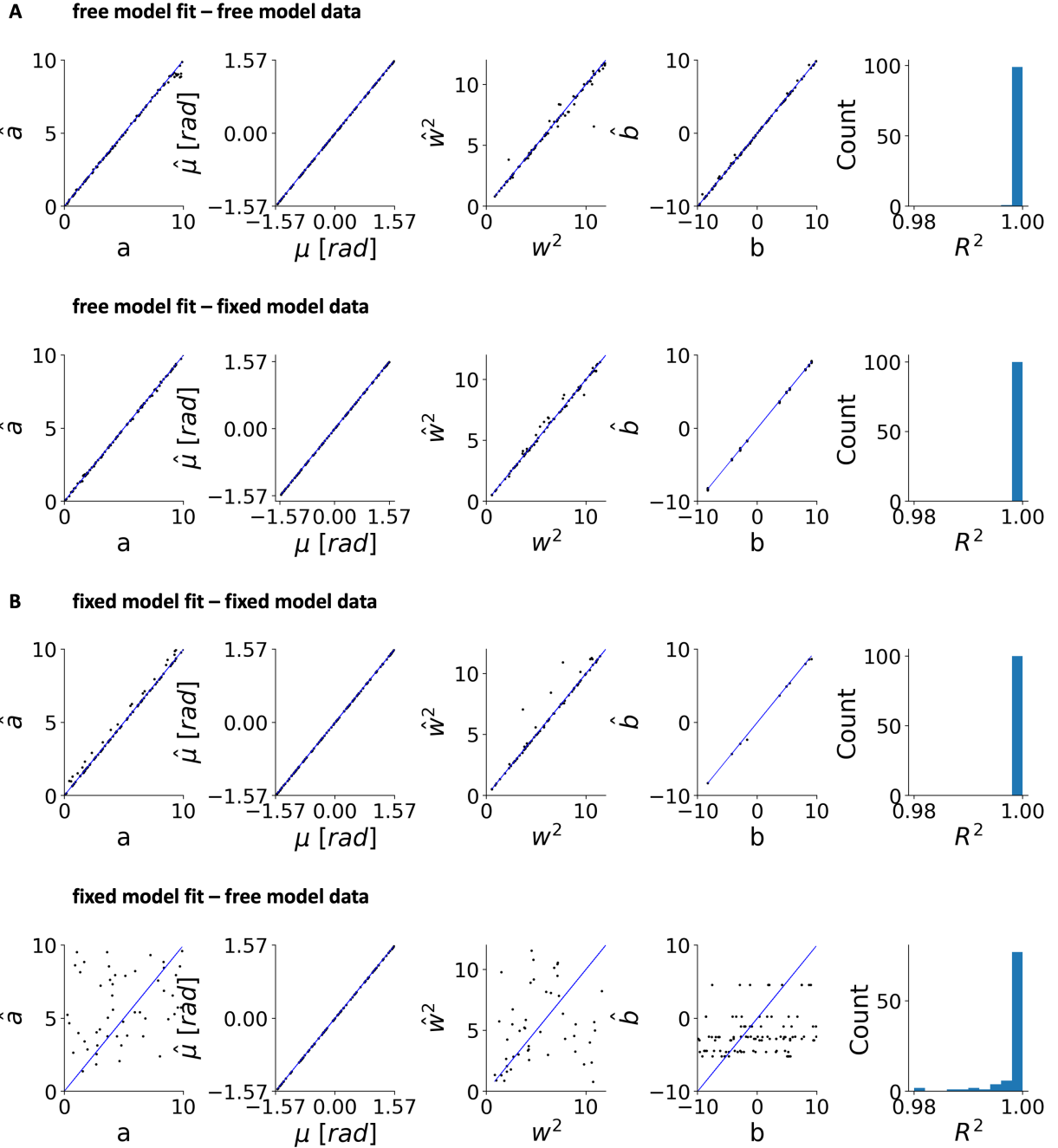


**Figure 4: Validation of Implemented Algorithms with Synthetic Data**  
True and estimated bump variable values on synthetic data generated from both models (100 samples) with a histogram of corresponding  $R^2$  values.  
(A) Free model optimisation    (B) Fixed model optimisation

Quality of fitting is measured by coefficient of determination (R-squared) evaluated at all time points

$$R^2(t) = 1 - \frac{\mathbb{E}_i[(V_i(t) - f_i(\omega(t)))^2]}{\text{Var}_i[V_i(t)]} \quad (24)$$

$R^2$  is the proportion of total variance in true data explained by the model. Higher  $R^2$  values indicates a better fit. Synthetic data were generated from the free model and the fixed model with random parameter values to test and validate the implemented optimisation algorithms (Figure 4). The free model optimisation was able to fit synthetic data generated from both the free and fixed model as validated by the scatter points close to the unity line and the high  $R^2$  values over 0.95 (Figure 4A). The fixed model optimisation was able to fit synthetic data generated from the fixed model and had restricted ability to estimate actual bump parameter values generated from the free model due to its constraint of constant baseline as expected (Figure 4B).

### 3.2 Bump Fit of Network Activity

The free and fixed model optimisation were applied to fit the bump equation to simulated network activity (Figure 5A and 5B). Estimated values of four variables  $a$ ,  $\mu$ ,  $w^2$  and  $b$  were extracted and  $R^2$  was computed at all time points (Figure 5C).

Both models could estimate the simulated membrane potential to a high accuracy with  $R^2$  values over 0.95 during the whole process (Figure 5A and 5C, bottom). The dynamics of estimated bump location  $\hat{b}$  was almost identical for the free and fixed models, indicating that both models captured the drift of activity bump. The estimated bump amplitude  $\hat{a}$  and baseline  $\hat{b}$  had similar spatial patterns but the free model showed slower transition from pre-stimulus phase to evoked phase. For estimated bump width  $\hat{w}^2$ , we observed a significant peak after stimulus onset for the fixed model (Figure 5C, right) compared to the free model (Figure 5C, left). This was caused by the sudden decrease of bump baseline  $b$  from the pre-stimulus phase to evoked phase. In the fixed model, we constrained the bump baseline to be constant in each phase so the baseline decreased to the constant value with no transition when the stimulus was applied. This would cause a large difference between estimated bump from the two models (Figure 6B, blue solid and blue dashed line). The bump width  $w^2$  was overestimated (Figure 6B, orange solid line) to minimise difference with the free model fit. This suggested us the limit of the fixed model fit, that network interactions resulted in slow transition of average neuronal activity when there was a rapid change in external input baseline. Thus, the free model optimisation was used to estimate bump parameter values and perform further analysis in Section 4.

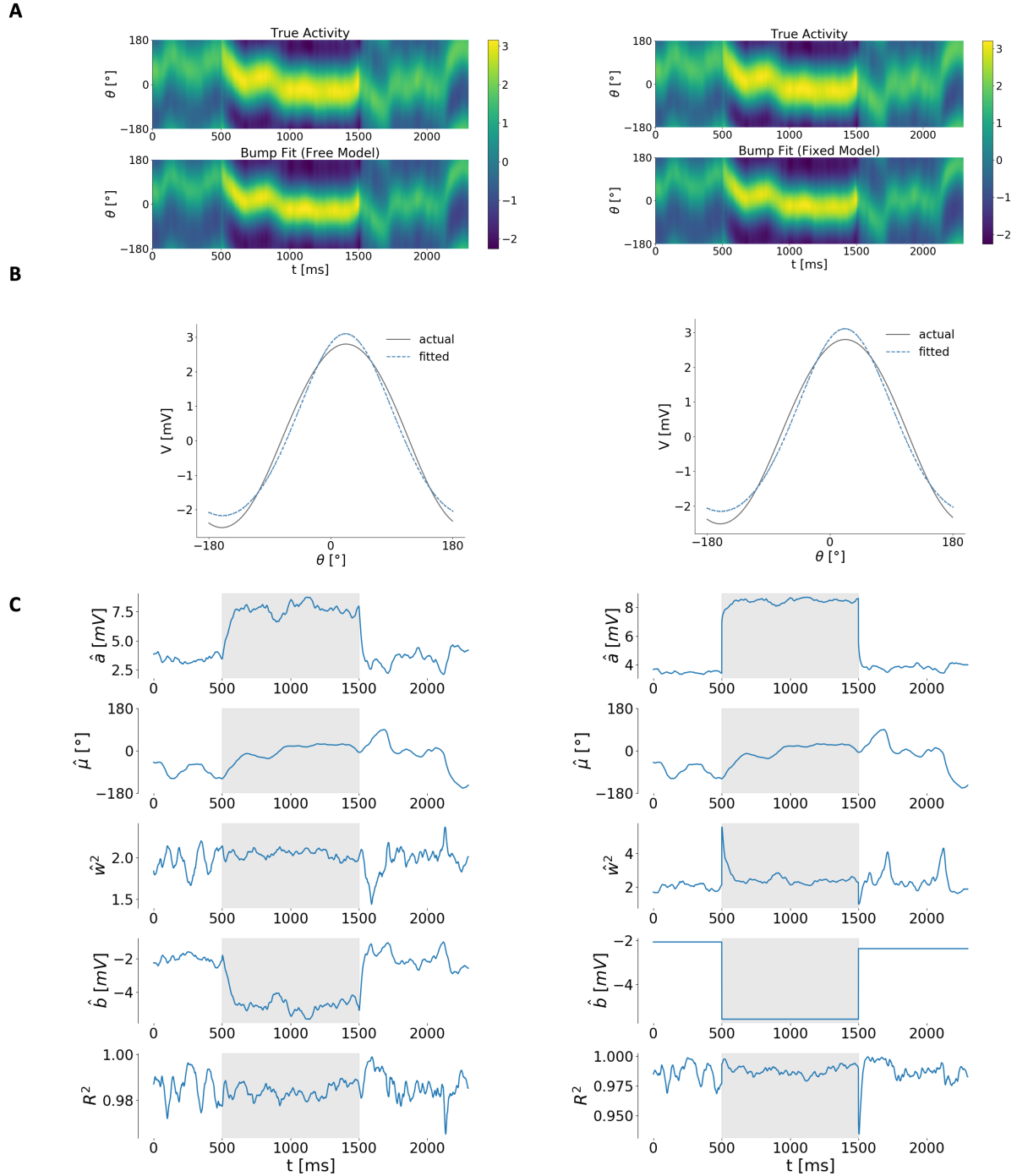


**Figure 5: Model Optimisation of Network Activity with Bump Equation**

(A) Free model (left) and fixed model (right) fit of true membrane potentials in network activity (same sample as in Figure 3).

(B) Sample true membrane potential and fitted circular Gaussian bump ( $t = 1000\text{ms}$ ).

(C) Dynamics of estimated bump parameters and  $R^2$  values computed at all time points.

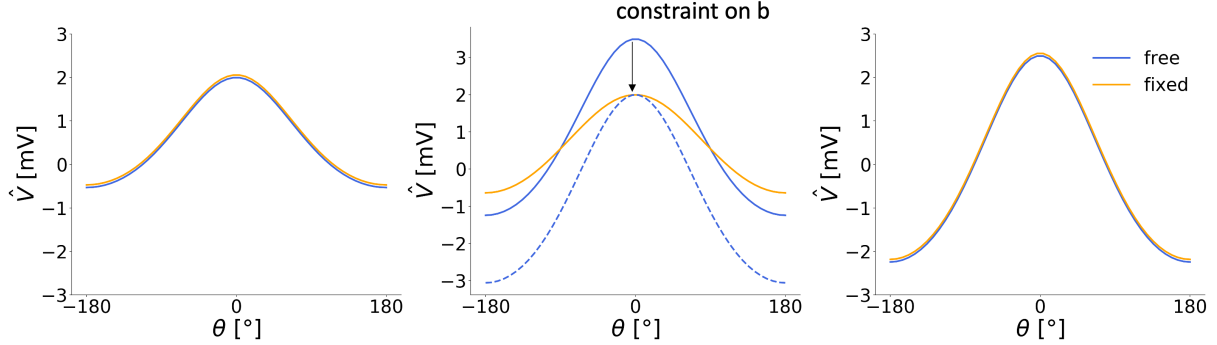


Figure 6: **Bump Transition from Pre-Stimulus Phase to Evoked Phase**

Estimated activity bumps in the pre-stimulus phase (left; same sample as in Figure 3,  $t \sim 490\text{ms}$ ), initial transition of evoked phase (middle;  $t \sim 520\text{ms}$ ) and evoked phase (right;  $t \sim 800\text{ms}$ ) using parameters values estimated from the free model (blue) and the fixed model (yellow). The blue dashed line marks the reconstructed bump using values of  $\hat{a}$ ,  $\hat{\mu}$  and  $\hat{w}^2$  from the fixed model and  $\hat{b}$  from the free model at the initial transition of evoked phase ( $t \sim 520\text{ms}$ ).

## 4 Network Dynamics and Variability Modelling

### 4.1 Statistics of Bump Parameters

Numerical simulations were performed to generate sample network activity for  $N_{trial}$  times and the free model optimisation was applied to fit the bump equation to membrane potentials for all time points in each trial

$$\begin{aligned}\hat{V}_i^n(t) &\approx f_i(\hat{\omega}_n(t)) \\ &= \hat{a}_n(t) \cdot \exp\left(\frac{\cos(\theta_i - \hat{\mu}_n(t)) - 1}{\hat{w}_n(t)^2}\right) + \hat{b}_n(t)\end{aligned}\quad (25)$$

where  $\hat{\omega}_n(t)$  denotes the estimated parameter vector of  $\omega(t)$  in  $n$ th trial.

Consistent with the single trial simulation (Figure 5C, left), the magnitude of bump amplitude increased in a short timescale when the stimulus is applied (Figure 7), representing the enhanced activity bump during evoked activity. The bump location fluctuated randomly between  $-180^\circ$  to  $180^\circ$  in the pre-stimulus phase. It converged to the stimulus orientation at  $0^\circ$  in a slightly longer timescale when the stimulus was applied (Figure 7, top), leading to a significant drop in across-trial variance of bump location during evoked activity (Figure 7, bottom right).

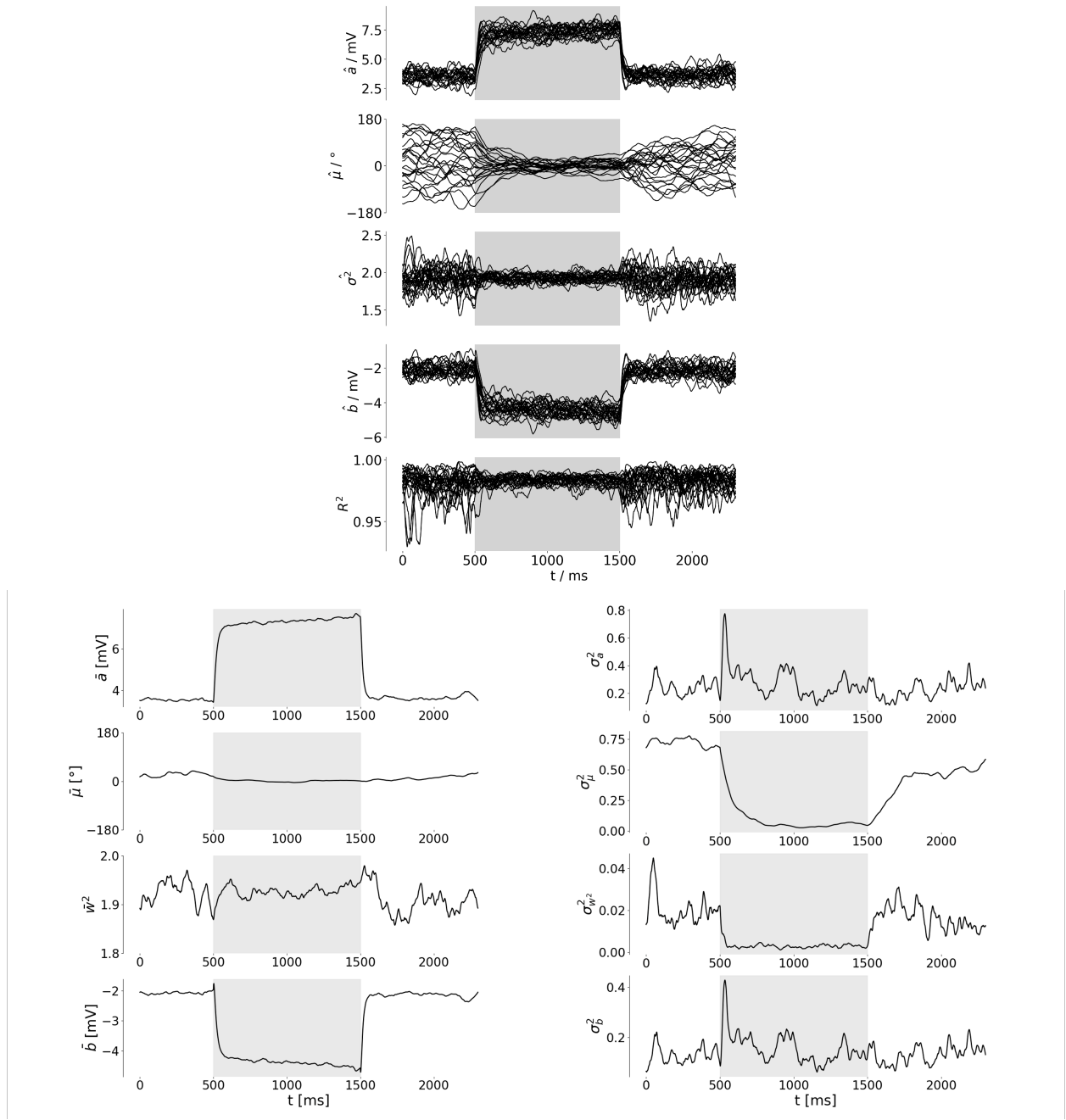


**Figure 7: Statistics of Estimated Bump Parameters**  
 Sample estimated variable and  $R^2$  values (top), across-trial mean (bottom left) and variance (bottom right) of four bump parameters ( $N_{\text{trial}} = 25$ ).

## 4.2 Variability Modelling with Bump Parameters

The across-trial variance is the second moment of membrane potentials. To understand dynamics of variability, we used the the first moment and second moment of bump parameters to model the across-trial variance  $\hat{\sigma}^2$ , given by

$$\hat{\sigma}^2(t) \approx \langle \text{Var}_n[\hat{V}_i^n(t)] \rangle_i \quad (26)$$

Three assumptions that focus differently on the bump and temporal dynamics were used to model the variance.

### Assumption 1. *Variability in $\mu$ only*

*The across-trial variability of only the bump location  $\mu$  is taken into account to estimate the membrane potentials in each trial*

$$\begin{aligned} \hat{V}_i^n(t) &\approx f_i(\bar{a}(t), \hat{\mu}_n(t), \bar{w}(t), \bar{b}(t)) \\ &= \bar{a}(t) \cdot \exp\left(\frac{\cos(\theta_i - \hat{\mu}_n(t)) - 1}{\bar{w}(t)^2}\right) + \bar{b}(t). \end{aligned} \quad (27)$$

*Other bump parameters are replaced by the across-trial average values  $\bar{\omega}(t)$ , i.e.  $\bar{\omega}(t) = \frac{1}{N_{\text{trial}}} \sum_{n=1}^{N_{\text{trial}}} \hat{\omega}_n(t)$ .*

### Assumption 2a. *Small variability (in all parameters and $\mu$ especially)*

*The bump location converges to the stimulus orientation and the across-trial variance of bump variables drops significantly when the stimulus is applied. Assuming the variability in bump variables is small, the information in local partial derivative could be used to model the across-trial variance. The first-order Taylor series is used to expand the bump equation (Equation 25) about the across-trial average value  $\bar{\omega}(t)$*

$$f_i(\hat{\omega}_n(t)) \approx f_i(\bar{\omega}(t)) + (\hat{\omega}_n(t) - \bar{\omega}(t)) \nabla_{\omega} f_i(\bar{\omega}(t)). \quad (28)$$

*The individual across-trial variance  $\hat{\sigma}_i^2$  for neuron  $i$  can be expressed as*

$$\begin{aligned} \hat{\sigma}_i^2(t) &= \text{Var}_n[f_i(\hat{\omega}_n(t))] \\ &= \text{Var}_n[\hat{\omega}_n(t) \nabla_{\omega} f_i(\bar{\omega}(t))] \\ &= [\nabla_{\omega} f_i(\bar{\omega}(t))]^\top \text{Cov}(\hat{\omega}) \nabla_{\omega} f_i(\bar{\omega}(t)) \\ &= \sum_{p=1}^4 (\alpha_i^{\omega_p}(t))^2 \sigma_{\hat{\omega}_p}^2(t) + \sum_{p=1}^4 \sum_{\substack{q=1 \\ p \neq q}}^4 (\alpha_i^{\omega_p}(t)) (\alpha_i^{\omega_q}(t)) \sigma_{\hat{\omega}_p \hat{\omega}_q}^2(t) \end{aligned} \quad (29)$$

where  $\sigma_{\hat{\omega}_p}(t) = \text{Var}_n [\hat{\omega}_p^n(t)]$  and  $\sigma_{\hat{\omega}_p \hat{\omega}_q}^2(t) = \text{Cov} [\hat{\omega}_p^n(t), \hat{\omega}_q^n(t)]$ . The coefficient  $\alpha_i^{\omega_p}$  is the coefficient in the first-order Taylor series expansion

$$\alpha_i^{\omega_p}(t) = \frac{\partial f_i(\boldsymbol{\omega}(t))}{\partial \omega_p(t)} (\bar{\omega}_p(t)). \quad (30)$$

The across trial variance is then computed by averaging across all neurons in the network

$$\hat{\sigma}^2(t) = \langle \hat{\sigma}_i^2(t) \rangle_i \quad (31)$$

### **Assumption 2b. Large variability in $\mu$ (uniform distribution)**

During spontaneous activity, the bump location fluctuates at random angular position and can be modelled as a random variable from uniform distribution between  $-\pi$  and  $\pi$ . The across-trial variance  $\hat{\sigma}^2$  the average of across-neuron averaged individual variance  $\hat{\sigma}_i^2$  estimated by

$$\begin{aligned} \hat{\sigma}_i^2(t) &= \text{Var}_{\mu}[f_i(\hat{a}(t), \mu, \hat{w}(t), \hat{b}(t))] \\ &= \mathbb{E}_{\mu}[f_i(\hat{a}(t), \mu, \hat{w}(t), \hat{b}(t))^2] - (\mathbb{E}_{\mu}[f_i(\hat{a}(t), \mu, \hat{w}(t), \hat{b}(t))])^2 \\ &= \int_{-\pi}^{\pi} (f_i(\hat{a}(t), \mu, \hat{w}(t), \hat{b}(t)))^2 \frac{1}{2\pi} d\mu - \left( \int_{-\pi}^{\pi} f_i(\hat{a}(t), \mu, \hat{w}(t), \hat{b}(t)) \frac{1}{2\pi} d\mu \right)^2. \end{aligned} \quad (32)$$

### **Assumption 3. Time dependency in $a$ and $\mu$ only**

The temporal variability of only the bump amplitude  $a$  and location  $\mu$  was taken into account to calculate membrane potentials in each trial

$$\hat{V}_i^n(t) \approx \hat{a}_n(t) \cdot \exp \left( \frac{\cos(\theta_i - \hat{\mu}_n(t)) - 1}{\hat{w}_n^2} \right) + \hat{b}_n. \quad (33)$$

Other bump parameters are replaced by their time average values  $\hat{\omega}_n$ , i.e.  $\hat{\omega}_n = \frac{1}{T} \sum_{t=1}^T \hat{\omega}_n(t)$ .

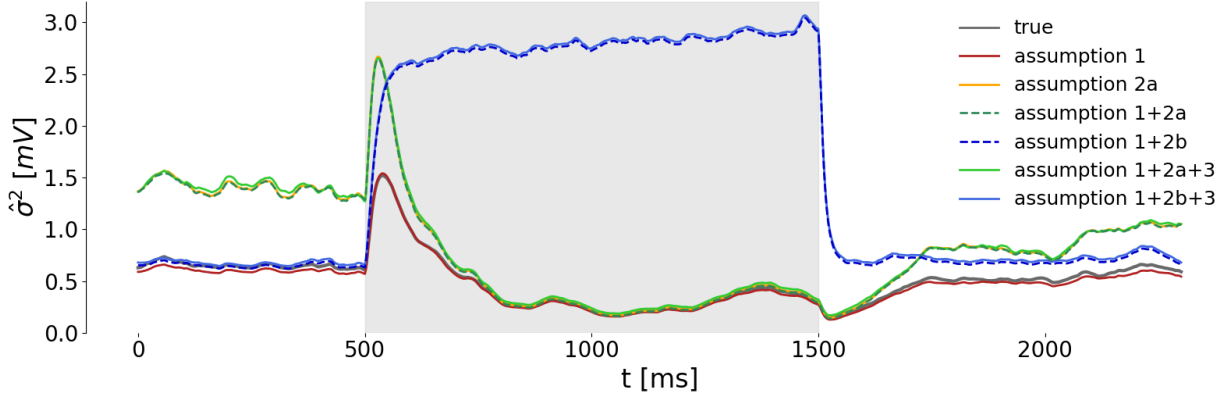


**Figure 8: Across-Trial Variance Reconstruction with Bump Parameters**  
 Sample reconstructed across-trial variance from estimated bump parameters under purposed assumptions (color coded;  $N_{\text{trial}} = 25$ , same samples as in Figure 7).

The across-trial variance was reconstructed under a single assumption or a combination of assumptions (Figure 8). Assumption 1 was strongly supported by the highly similar reconstructed variance to the true variance (Figure 8, red and grey line) through the whole process. Assumption 3 was also supported since combining Assumption 1 or 3 to other assumptions produced little change on the reconstructed variance. They showed that the across-trial variability in the ring attractor model was mainly caused by the spatial and temporal variability in bump amplitude and location. Assumption 2a and 2b hold respectively depending on the presence of stimulus. The reconstructed variance under Assumption 2a (Figure 8, green solid line) initially overestimated the variance in the pre-stimulus phase and converged to the true value during evoked activity. The accuracy of reconstructed variance under Assumption 2b (Figure 8, blue solid line) was high during spontaneous activity and remained high for a short period after stimulus applied. In other words, Assumption 2b and 2a are valid in spontaneous activity and evoked activity respectively. The shift in accuracy from Assumption 2b to 2a was due to the bump location dynamics that the activity bump transits from a random location to the stimulus orientation (Figure 7, top). Note that the reconstructed variance under small variability assumption (Assumption 2a) also showed the initial variance increase at stimulus onset as the true variance.

### 4.3 Relations to Network Dynamics

The initial variance increase at stimulus onset is investigated by analysing the reconstructed variance under combined Assumption 1, 2a and 3, which is the product of squared coefficient averaged across neurons and the variance of estimated bump location

$$\begin{aligned}\hat{\sigma}^2(t) &= \langle (\alpha_i^\mu(t))^2 \cdot \sigma_{\hat{\mu}}^2(t) \rangle_i \\ &= \langle (\alpha_i^\mu(t))^2 \rangle_i \cdot \sigma_{\hat{\mu}}^2(t).\end{aligned}\quad (34)$$

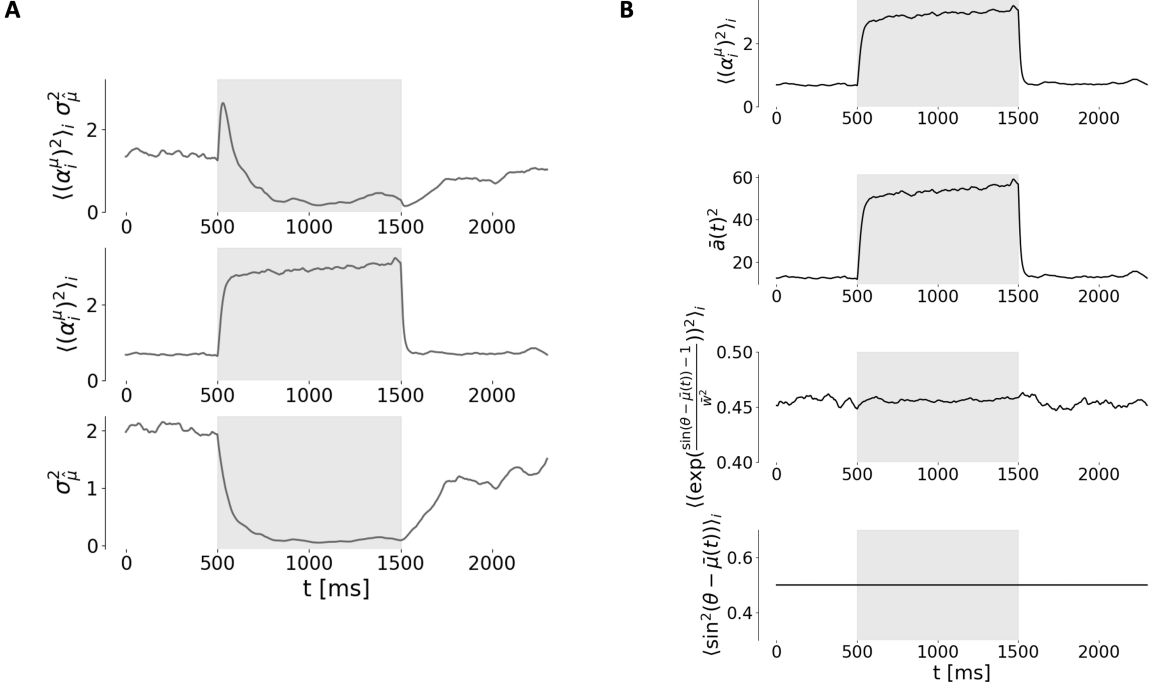


**Figure 9: Variance Reconstruction under Combined Assumptions 1+2a+3**  
(A) Reconstructed variance as the product of averaged squared coefficient and variance of bump location (Equation 34) under combined assumptions 1+2a+3 ( $N_{\text{trial}} = 25$ , same samples as in Figure 7).  
(B) Squared coefficient averaged across neurons as the product of three individual components (Equation 36).

The coefficient  $\alpha_i^\mu$  is the coefficient of first-order Taylor series (Equation 30), given by

$$\begin{aligned} \alpha_i^\mu(t) &= \frac{\partial f_i(\omega(t))}{\partial \mu(t)}(\bar{a}(t), \bar{\mu}(t), \bar{w}, \bar{b}) \\ &= \bar{a}(t) \cdot \exp\left(\frac{\cos(\theta_i - \bar{\mu}(t)) - 1}{\bar{w}^2}\right) \cdot \frac{1}{\bar{w}^2} \cdot \sin(\theta_i - \bar{\mu}(t)) \cdot (-1) \end{aligned} \quad (35)$$

where  $\bar{w}$  is the time and across-trial average of estimated parameter  $\hat{\omega}_n(t)$ , i.e.  $\bar{w} = \frac{1}{N_{\text{trial}} T} \sum_{n=1}^{N_{\text{trial}}} \sum_{t=1}^T \hat{\omega}_n(t)$ . The reconstructed variance is then proportional to four components

$$\hat{\sigma}^2(t) \propto \bar{a}(t)^2 \cdot \left\langle \exp\left(\frac{\cos(\theta_i - \bar{\mu}(t)) - 1}{\bar{w}^2}\right) \right\rangle_i \cdot \langle \sin^2(\theta_i - \bar{\mu}(t)) \rangle_i \cdot \sigma_\mu^2(t). \quad (36)$$

The exponential and squared sine components were found to be roughly constant through the process (Figure 9B) so temporal dynamics of reconstructed variance mainly depended on the magnitude of bump amplitude and across-trial variance of bump location  $\sigma_\mu^2$

$$\hat{\sigma}^2(t) \propto \bar{a}(t)^2 \cdot \sigma_\mu^2(t). \quad (37)$$

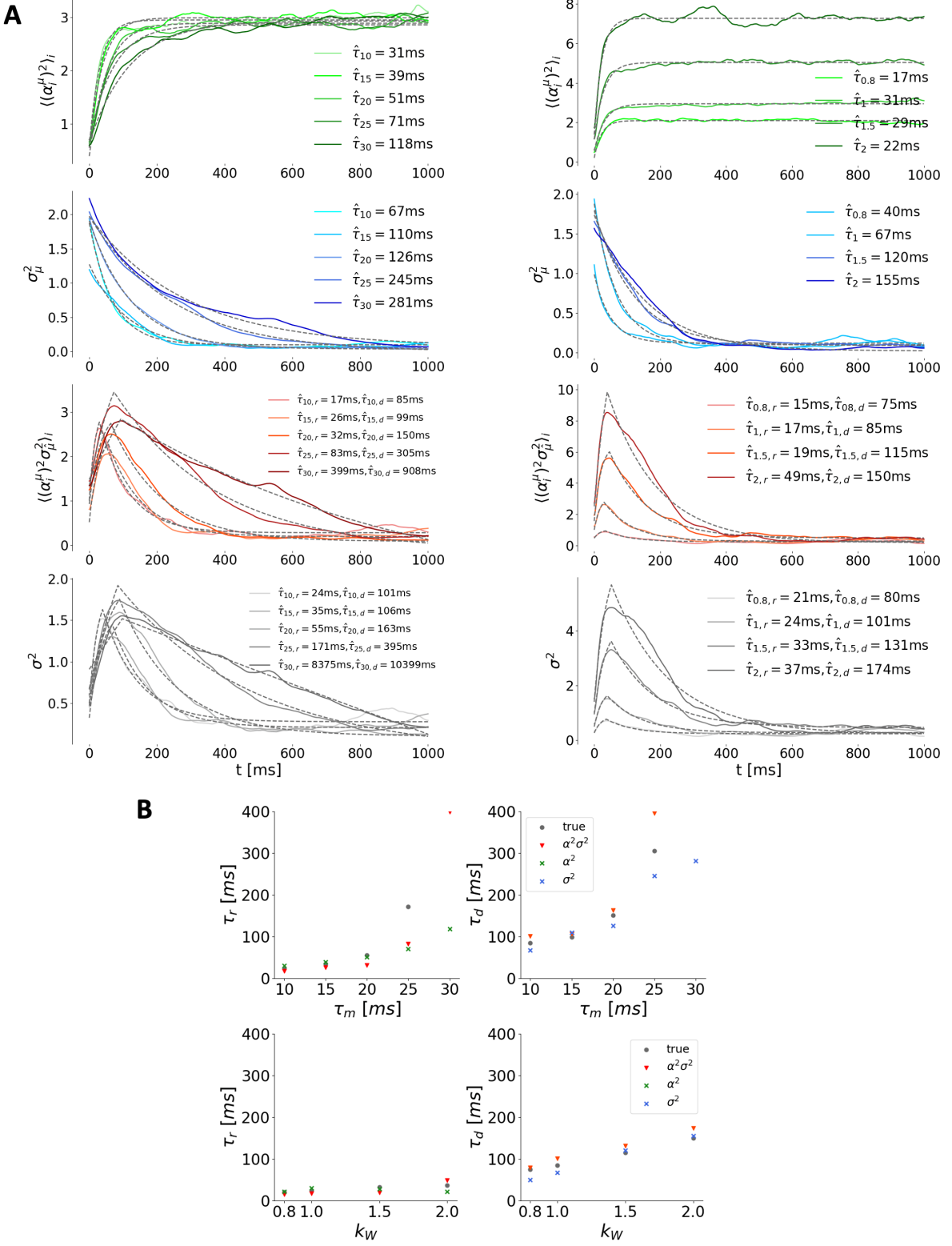


Figure 10: **Across-Trial Variance Reconstruction with Bump Parameters**

(A) Fitting exponential decay to true variance, reconstructed variance as the product of two individual components for different membrane constants (left) and network weights (right; estimated time constant marked in the plot).

(B) Scatter plot of estimated time constants.

To obtain time constant of the transition, the true across-trial variance  $\sigma^2$ , reconstructed variance  $\hat{\sigma}^2$  under combined assumption 1+2a+3, averaged squared coefficient  $\langle(\alpha_i^\mu)^2\rangle_i$  and variance of bump location  $\sigma_{\hat{\mu}}^2$  during evoked activity is each fitted to an exponential decay equation. Note that the true and reconstructed variance was fitted to a function that rises up to the maximum value at transition point  $t = t_{\text{tr}}$  then decays until the end of evoked activity

$$f(t; a_r, b_r, \tau_r, b_d, \tau_d, t_{\text{tr}}) = \begin{cases} a_r (1 - e^{-\frac{t}{\tau_r}}) + b_r, & 0 < t \leq t_{\text{tr}} \\ (a_r (1 - e^{-\frac{t_{\text{tr}}}{\tau_r}}) + b_r - b_d) e^{-\frac{t-t_{\text{tr}}}{\tau_d}} + b_d, & t_{\text{tr}} < t \leq T \end{cases}$$

Continuity of the fitted variance is ensured by choosing decaying amplitude  $a_d$  so that function value at both sides are equal at the transition point.

Network simulations and variance modelling were performed over a range of membrane time constants  $\tau_m$  and network weights  $W'_{ij} = k_w \cdot W_{ij}$  scaled by a constant  $k_w$ . The rising averaged squared coefficient  $\langle(\alpha_i^\mu)^2\rangle_i$  was much faster than the decaying bump location variance  $\sigma_{\hat{\mu}}^2$  under all parameter settings (Figure 10A). The averaged squared coefficient rose significantly in a short time scale as the result of increasing bump amplitude, while variance of bump location dropped slowly due to its movement from a random location to the stimulus orientation (Figure 9A). The reconstructed variance, which is proportional to the product two terms (Equation 34), then would show an initial peak before the magnitude decreases. We observed that change in membrane time constant  $\tau_m$  led to significant change in rising time constant  $\tau_r$  and decaying time constant  $\tau_d$  of all quantities (Figure 10B). This is because membrane time constant directly modulates the rate of change of membrane potential (Equation 8) and its variance. The network weight  $W'_{ij}$  occurs in the recurrence term so will affect the decaying time constant as a result of network dynamics (Equation 1). The rising change of rate mainly depends on the membrane potential term  $V_i$  and is not strongly affected by the recurrence relationship.

## 5 Future Work

### 5.1 Large Scale Simulations

This project analysed the statistics of the membrane potential under repeated trials. Analysis in section 4 was based on network simulation and modelling of 25-30 trials under each network parameter setting, limited by computational load of our analysis (especially parameter estimation) and computational power of my laptop. The project findings could be verified and further investigated by running larger numbers of simulation over a wider range of network parameter settings.

## 5.2 Generalising Analysis

So far, the ring attractor model with symmetrical network weights  $W_{ij}$  across all neurons (Equation 2) was used for the project. This is an example of the continuous multi-attractor model. Similar analysis on variability could be applied to the discrete multi-attractor model by adding a noise term to break the symmetry in network weight. Spatial patterns of neural activity in the discrete multi-attractor network do not naturally form to a bump at stimulus onset (Seeholzer et al., 2019). Other methods might need to be used to model network activity and analyse across-trial variability.

## 6 Conclusions

In the report, we investigated the across-trial variability in the ring attractor model. We developed procedures to simulate and model the membrane potentials. We found that the spatial and temporal dynamics of across-trial variance was mainly due to increased activity bump and convergence of bump location to the stimulus orientation. This project supported the usefulness of modelling and understanding the network activity using circular Gaussian bump, and could be used for further analysis of the multi-attractor model under different network settings.

## 7 Appendix

### 7.1 Network Parameters Used in Numerical Simulations

The values of all the parameters used for simulations in Section 2–4 are listed in the table below.

Symbol	Value	Unit	Description
$N$	100	-	Number of neurons
$\tau_m$	10	ms	Membrane time constant
$k$	0.1	$\text{mV}^{-1}$	Non-linearity gain
$g_{\max}$	100	$\text{s}^{-1}$	Maximal firing rate
$\bar{W}$	$-40/g_{\max}$	$\text{mV}\cdot\text{s}$	Average connection weight
$W_\Delta$	$33/g_{\max}$	$\text{mV}\cdot\text{s}$	Tuning-dependent modulation of connection weight
$\tau_{\text{noise}}$	50	ms	Noise correlation time constant
$\sigma_0$	0.15	mV	Noise standard deviation
$l_{\text{noise}}$	60	deg.	Noise correlation length scale
$b_0$	2	mV	Input baseline
$A$	0.1	mV	Depth of input tuning
$\theta_{\text{stim}}$	0	deg.	Stimulus direction

Table 1: Parameters Used for Ring Attractor Model Simulations

## 7.2 Mathematical Formulations

### 7.2.1 The Forward Euler Scheme

Consider a differential equation  $\frac{dy}{dx} = f(x, y)$ , the process  $y$  is approximated by

$$y_{n+1} \approx y_n + h f(x_n, y_n) \quad (38)$$

where  $x_{n+1} = x_n + h$  and increment  $h$  is the step size.

### 7.2.2 Partial Derivatives of Objective Function to Bump Variables

The partial derivative of objective function (Equation 17) with respect to  $\hat{a}$ ,  $\hat{\mu}$  and  $\hat{w}^2$  can be computed at a time point  $t$  respectively (symbol  $t$  in bump variables and membrane potential is neglected)

$$\frac{\partial L(\hat{\omega}_{1:T})}{\partial \hat{a}} = -\frac{2}{NT} \sum_{i=1}^N \left[ V_i - \hat{a} \cdot \exp\left(\frac{\cos(\theta_i - \hat{\mu}) - 1}{\hat{w}^2}\right) - \hat{b} \right] \cdot \exp\left(\frac{\cos(\theta_i - \hat{\mu}) - 1}{\hat{w}^2}\right) \quad (39)$$

$$\begin{aligned} \frac{\partial L(\hat{\omega}_{1:T})}{\partial \hat{\mu}} &= \\ \frac{2}{NT} \sum_{i=1}^N \frac{\hat{a}}{\hat{w}^2} \left[ V_i - \hat{a} \cdot \exp\left(\frac{\cos(\theta_i - \hat{\mu}) - 1}{\hat{w}^2}\right) - \hat{b} \right] \cdot \exp\left(\frac{\cos(\theta_i - \hat{\mu}) - 1}{\hat{w}^2}\right) \cdot \sin(\theta_i - \hat{\mu}) \end{aligned} \quad (40)$$

$$\begin{aligned} \frac{\partial L(\hat{\omega}_{1:T})}{\partial \hat{w}^2} &= \\ \frac{4}{NT} \sum_{i=1}^N \frac{\hat{a}}{\hat{w}^3} \left[ V_i - \hat{a} \cdot \exp\left(\frac{\cos(\theta_i - \hat{\mu}) - 1}{\hat{w}^2}\right) - \hat{b} \right] \cdot \exp\left(\frac{\cos(\theta_i - \hat{\mu}) - 1}{\hat{w}^2}\right) \cdot \cos(\theta_i - \hat{\mu}) \end{aligned} \quad (41)$$

The partial derivative with respect to  $\hat{b}$  is computed differently for the fixed and the free model as in Section 3.1.

### 7.3 Data and Software Availability

The code used for model simulations and data analysis is available in Github (<https://github.com/yuetongc/multi-attractor-network>).

### 7.4 Health and Safety Retrospective

A risk assessment form was completed before the start of this project. No risk or hazard was identified in the assessment form and was found during the project since this project is programming based.

### 7.5 COVID-19 Disruption

The COVID-19 epidemics from March 2020 have significantly disrupted the university's operation and teaching. There had been no major physical disruption to this project's progress as project work mainly involved mathematical modelling and computer programming. Regular online meetings were scheduled with my supervisor to discuss the weekly results. The only minor disruption is the level of stress and anxiety due to outbreak in the UK and lack of outdoor activities. This had reduced my work efficiency in conducting project work in Easter term and writing the final report.

## References

- [1] Ben-Yishai, R., Bar-Or, R.L., Sompolinsky, H. (1995). *Theory of orientation tuning in visual cortex*. Proc. Natl. Acad. Sci. USA 92, 3844–3848.
- [2] Churchland, M.M., Yu, B.M., Cunningham, J.P., Sugrue, L.P., Cohen, M.R., Corrado, G.S., Newsome, W.T., Clark, A.M., Hosseini, P., Scott, B.B., et al. (2010). *Stimulus onset quenches neural variability: a widespread cortical phenomenon*. Nat. Neurosci. 13, 369–378.
- [3] Deco, G., Hugues, E. (2012). *Neural network mechanisms underlying stimulus driven variability reduction*. PLoS Comput. Biol. 8, e1002395.
- [4] Hennequin, G., Ahmadian, Y., Rubin, D. B., Lengyel, M., Miller, K. D. (2018). *The dynamical regime of sensory cortex: stable dynamics around a single stimulus-tuned attractor account for patterns of noise variability*. Neuron, 98(4), 846-860.
- [5] Kim, S.S., Rouault, H., Druckmann, S., Jayaraman, V. (2017). *Ring attractor dynamics in the Drosophila central brain*. Science, 356, 849-853.
- [6] Litwin-Kumar, A., Doiron, B. (2012). *Slow dynamics and high variability in balanced cortical networks with clustered connections*. Nat. Neurosci. 15, 1498–1505.
- [7] Ponce-Alvarez, A., Thiele, A., Albright, T. D., Stoner, G. R., and Deco, G. (2013). *Stimulus-dependent variability and noise correlations in cortical MT neurons*. Proceedings of the National Academy of Sciences, 110(32), 13162-13167.
- [8] Seeholzer, A., Deger, M., Gerstner, W. (2019). *Stability of working memory in continuous attractor networks under the control of short-term plasticity*. PLoS Comput. Biol. 15(4), e1006928.
- [9] Seung, H.S. (1996). *How the brain keeps the eyes still*. Proc. Natl. Acad. Sci. USA, 93: 13339-13344.
- [10] Wimmer, K., Nykamp, D. Q., Constantinidis, C. & Compte, A. (2014). *Bump attractor dynamics in prefrontal cortex explains behavioral precision in spatial working memory*. Nat. Neurosci. 17, 431–439.
- [11] Zhang, K. (1996). *Representation of Spatial Orientation by the Intrinsic Dynamics of the Head-Direction Cell Ensemble: A Theory*. J. Neurosci. 16, 2112–2126.